Original Article

Endoscopic optical coherence tomography angiography using inverse SNR-amplitude decorrelation features and electrothermal micro-electro-mechanical system raster scan

Lin Yao[1#], Huakun Li[1#], Kaiyuan Liu[1], Ziyi Zhang[1], Peng Li[1,2,3,4]^

[1]State Key Laboratory of Modern Optical Instrumentation, College of Optical Science and Engineering, Zhejiang University, Hangzhou, China; [2]Jiaxing Key Laboratory of Photonic Sensing & Intelligent Imaging, Jiaxing, China; [3]Intelligent Optics & Photonics Research Center, Jiaxing Research Institute, Zhejiang University, Jiaxing, China; [4]Hebei Key Laboratory of Micro-Nano Precision Optical Sensing and Measurement Technology, Qinhuangdao, China

Contributions: (I) Conception and design: L Yao, H Li, P Li; (II) Administrative support: P Li; (III) Provision of study materials or patients: L Yao, H Li, P Li; (IV) Collection and assembly of data: All authors; (V) Data analysis and interpretation: L Yao, H Li, P Li; (VI) Manuscript writing: All authors; (VII) Final approval of manuscript: All authors.

[#]These authors contributed equally to this work.

Correspondence to: Peng Li. College of Optical Science and Engineering, Zhejiang University, Hangzhou 310027, China. Email: Peng_Li@zju.edu.cn.

Background: Angiogenesis is closely associated with tumor development and progression. Endoscopic optical coherence tomography angiography (OCTA) enables rapid inspection of mucosal 3D vasculature of inner organs in the early-stage tumor diagnosis; however, it is limited by instabilities of the optical signal and beam scanning.

Methods: In the phase-unstable swept source OCTA (SS-OCTA), amplitude decorrelation was used to compute the motion-induced changes as motion contrast. The influence of the random noise-induced amplitude fluctuations on decorrelation was characterized as a function of inverse signal-to-noise ratio (SNR) with a multi-variate time series (MVTS) model and statistical analysis. Then, the noise-induced decorrelation artifacts in static tissue regions were eliminated by applying a flow mask based on the statistical relation between inverse SNR (iSNR) and amplitude decorrelation (IDa), which was named IDa-OCTA. In addition, a distal stepwise raster scan was realized with a low-voltage electrothermal micro-electro-mechanical system (ET-MEMS)-based catheter for endoscopic imaging, whereby the stable and repeatable B-scans at each step suppressed the decorrelation noise induced by the spatial mismatch between paired scans.

Results: The derived IDa relation was validated through numerical simulation and flow phantom experiments. *In vivo* human buccal mucosa imaging was performed to demonstrate the endoscopic IDa-OCTA imaging. In this, the subsurface structure and vasculature were visualized in a rapid and depth-resolved manner.

Conclusions: The rapid 3D vasculature visualization realized by the endoscopic IDa-OCTA improves the diagnosis of early tumors in internal organs.

Keywords: Biomedical imaging; electrothermal micro-electromechanical system (ET-MEMS); endoscopic optical coherence tomography angiography (OCTA)

Submitted Oct 29, 2021. Accepted for publication Mar 11, 2022.
doi: 10.21037/qims-21-1056
View this article at: https://dx.doi.org/10.21037/qims-21-1056

^ ORCID: 0000-0002-9652-2369.

Introduction

Angiogenesis is closely associated with tumor development and progression (1). Using microvascular changes as an indicator of early-stage cancer, narrow band imaging (NBI) and confocal laser endomicroscopy (CLE) have been used for vascular imaging of the inner surface of luminal organs (2,3). However, NBI visualizes superficial vasculature with a limited resolution, while CLE achieves a relatively small field of view (FOV) and requires exogenous contrast agents. As a functional extension of optical coherence tomography (OCT) structural imaging, OCT angiography (OCTA) enables label-free and rapid visualization of subsurface 3D microvasculature down to capillary level by taking moving red blood cells (RBCs) as intrinsic contrast (4-6), and has been used to evaluate the presence of tumor vessels, vascular patterns, and vascular density in ophthalmology (7-9). In addition, the use of endoscopic OCTA has been proposed for the early cancer diagnosis of internal organs, such as the gastrointestinal (GI) tract (10,11). However, high quality OCTA imaging requires high stability of both optical signal and beam scanning, which is particularly challenging for a miniature probe.

A stable interference signal is needed to compute the motion contrast in OCTA. However, in the swept source OCTA (SS-OCTA) system, the phase component is unstable and hardly used for motion contrast calculation. Therefore, amplitude decorrelation is widely used in SS-OCTA to compute the motion-induced changes (5,12,13). However, random system noise (such as shot noise and thermal noise) induces additional amplitude fluctuations and generates noise-induced decorrelation artifacts, which severely degrade vascular visibility, particularly in low signal-to-noise ratio (SNR) regions (e.g., deep layers) (14-16). An asymptotic linear relation of inverse SNR (iSNR) to complex-signal decorrelation (ID) has been mathematically derived for SNR-adaptive angiographic imaging (6); however, the characteristics of the complex-based and amplitude-based OCT signals are different and are affected differently by the additive noise. Accordingly, the complex-based ID relation cannot be directly applied to the amplitude decorrelation-based OCTA, and an understanding of the dependence between iSNR and amplitude decorrelation (IDa) is needed to effectively suppress the amplitude decorrelation artifacts.

Additionally, the spatial mismatch between paired scans induces a severe decorrelation noise in the tissue background; a stable, precise, and repeatable scanning mechanism is required. Traditional proximal actuation produces nonuniform rotational and longitudinal distortion (17-19). Comparatively, the distal actuation would be more impervious to bending distortion. A micromotor has been used for a rotary (circumferential) scan at the distal end (20) and additional longitudinal scan mechanisms, such as proximal pullback (10,21) and pneumatic distal scanners (22), can be combined for large FOV volumetric imaging. Reports show that integration of a micromotor scanner and a piezoelectric resonant fiber scanner can generate a 2D cycloid pattern and a 1 mm× 38 mm strip OCTA image with a tethered capsule (23). However, although the side-viewing circumferential scanning has a large FOV, it has an inefficient imaging speed when targeting small regions flagged on endoscopic view which require closer inspection (24).

To meet the requirement of close-up inspection, Liang *et al.* (24) used a piezoelectric tubular actuator to produce 2D spiral scanning with a 450 μm FOV in diameter at the distal end, where the probe diameter was 3.3 mm and the rigid head length was 20 mm. The OCTA motion contrast was computed based on inter-volume changes (24), but the long inter-volume time (200 ms) was prone to severe motion artifacts and had an inferior vascular contrast. By incorporating a plano-convex lens, the distal piezoelectric tubular scanner reported by Wurster *et al.* (25) has a short rigid length of 11.3 mm, a diameter of 4 mm, and a FOV of up to 1.3 mm in diameter. However, in the spiral scanning, the sequential circular scans have different radii and spatial sampling, therefore additional decorrelation noise might be a challenge in the inter-frame (circle) OCTA (25). In addition, the spiral scan inefficiently samples toward the center and requires frequent trajectory calibration due to amplitude-dependent phase variation of the fiber scanner.

In contrast to the above-mentioned cycloid and spiral scanning patterns, a stepwise raster scanning pattern is preferred for the extraction of motion contrast from repeated B-scans, with minimal decorrelation noise in the background tissue. To generate a stable and controllable raster scanning pattern at the distal end, micro-electro-mechanical system (MEMS)-based beam scanners are an obvious choice. Compared with the electromagnetic MEMS with a relatively large volume (26), and the electrostatic MEMS with a limited scanning range (27), electrothermal (ET) MEMS has the advantages of compact size and larger deflection angle with relatively lower driving voltage (28,29).

In this work, we proposed an endoscopic SNR-adaptive SS-OCTA with an ET MEMS raster scan. First, we derived the theoretical IDa relation and accordingly proposed an

SNR-adaptive IDa-OCTA method to suppress the noise-induced decorrelation artifacts in the phase-unstable SS-OCTA system. Second, we reported on a lab-built endoscopic SS-OCTA system along with a low-voltage ET MEMS catheter, the stepwise raster scanning protocol, and the correction method for nonlinear distortion in ET MEMS. We then validated the theoretically derived IDa relation through numerical simulation and flow phantom experiments, and conducted *in vivo* endoscopic IDa-OCTA imaging in human buccal mucosa. Finally, the potential applications and limitations of this study were discussed. We present the following article in accordance with the MDAR checklist (available at https://qims.amegroups.com/article/view/10.21037/qims-21-1056/rc).

Methods

Statistical characteristics of OCT signals

Prior to statistically characterizing the amplitude decorrelation, we first derived the generalized probability density functions (PDFs) of the OCT amplitude. Leveraging the dissimilarity calculation between repeated frames, decorrelation-based angiography is insensitive to the multiplicative noise induced by overall variation of the light source intensity (30). Therefore, the complex-valued resultant OCT signal $\tilde{X}$ was defined as the sum of the noiseless true OCT signal $\tilde{A}$ and an additive white Gaussian noise $\tilde{n}$ (14,31-33), i.e.:

$$\tilde{X} = \tilde{A} + \tilde{n} \quad [1]$$

where $\tilde{A} \sim N\left(0, v^2\right)$ is the spatial speckle field produced by the coherent summation of light waves with random path lengths, and $\tilde{n} \sim N\left(0, s^2\right)$ represents detection noise, both of which follow a complex Gaussian distribution. Here, v^2 and s^2 are the variances of the speckle field and random noise, respectively (14). The resultant OCT signal obeys the following assumptions, which generally hold for measured samples: (I) the random noise $\tilde{n}$ is uncorrelated with true OCT signal $\tilde{A}$; (II) in dynamic regions, the speckle field is time-variant. Accordingly, for totally dynamic signals, we assume that $\tilde{A}$ obeys the same independent and identical distribution in temporal and spatial dimensions. (III) In static regions, the speckle field is stable, so the corresponding noiseless OCT signal $\tilde{A}$ is invariant in the temporal dimension.

To simplify the PDFs of OCT signals that will be involved in the following theoretical derivation, we use the noise level to normalize the amplitude of OCT signals. Herein, $x_0 = \frac{|\tilde{X}|}{s}$ and $a_0 = \frac{|\tilde{A}|}{s}$ are defined as the normalized amplitude of the resultant and noiseless OCT signal, respectively. Accordingly, the SNR defined as $\frac{E\left[|\tilde{X}|^2\right]}{E\left[|\tilde{n}|^2\right]} = \frac{s^2+v^2}{s^2}$ is also equal to the mean value of x_0^2, and iSNR is defined as the reciprocal of SNR, i.e., $iSNR = \frac{s^2}{s^2+v^2}$.

Based on these notations, a_0 follows a Rayleigh distribution in the spatial dimension denoted by $p_{A_0}(a_0)$, while for the OCT signal in the static region, x_0 follows a Rice distribution in the temporal dimension (34) (see detailed derivations in Appendix 1):

$$p_{A_0}\left(a_0\right) = \frac{2iSNR \cdot a_0}{1-iSNR} e^{-\frac{iSNR}{1-iSNR}a_0^2} \quad [2]$$

$$p_{X_0|A_0=a_0}\left(x_0\right) = 2x_0 e^{-x_0^2-a_0^2} I_0\left(2x_0 a_0\right) \quad [3]$$

where $p_{X_0|A_0=a_0}(x_0)$ means the PDF of x_0 when the normalized amplitude of noiseless OCT signal a_0 is a constant, and $I_0(\cdot)$ is the zeroth-order modified Bessel function of the first kind.

IDa asymptotic relation

Second, the IDa asymptotic relation was derived based on a multi-variate time series (MVTS) model from the perspective of mathematical expectation. In the phase-unstable SS-OCTA, amplitude-based inter-scan decorrelation was computed to estimate the motion magnitude of RBCs with a spatio-temporal kernel (5,6):

$$D = 1 - \frac{C}{I} = 1 - \frac{\sum_{m=1}^{M}\sum_{t=1}^{T-1} x_0(m,t)\, x_0(m,t+1)}{\sum_{m=1}^{M}\sum_{t=1}^{T-1} \frac{x_0^2(m,t) + x_0^2(m,t+1)}{2}} \quad [4]$$

where $x_0(m,t)$ denotes the normalized amplitude of the resultant OCT signal, C is the local first-order auto-covariance, and I is the local zeroth-order auto-covariance, which is generally called the intensity. As shown in *Figure 1A*, m is the spatial index with a total kernel size of M in 3 spatial dimensions, and t is the temporal index with total T repeated B-scans at each location.

Based on the MVTS model and the time series theory presented by Huang *et al.* and Cavazoscadena (6,35), when the total spatio-temporal kernel size $N=M\times T$ approaches infinity,

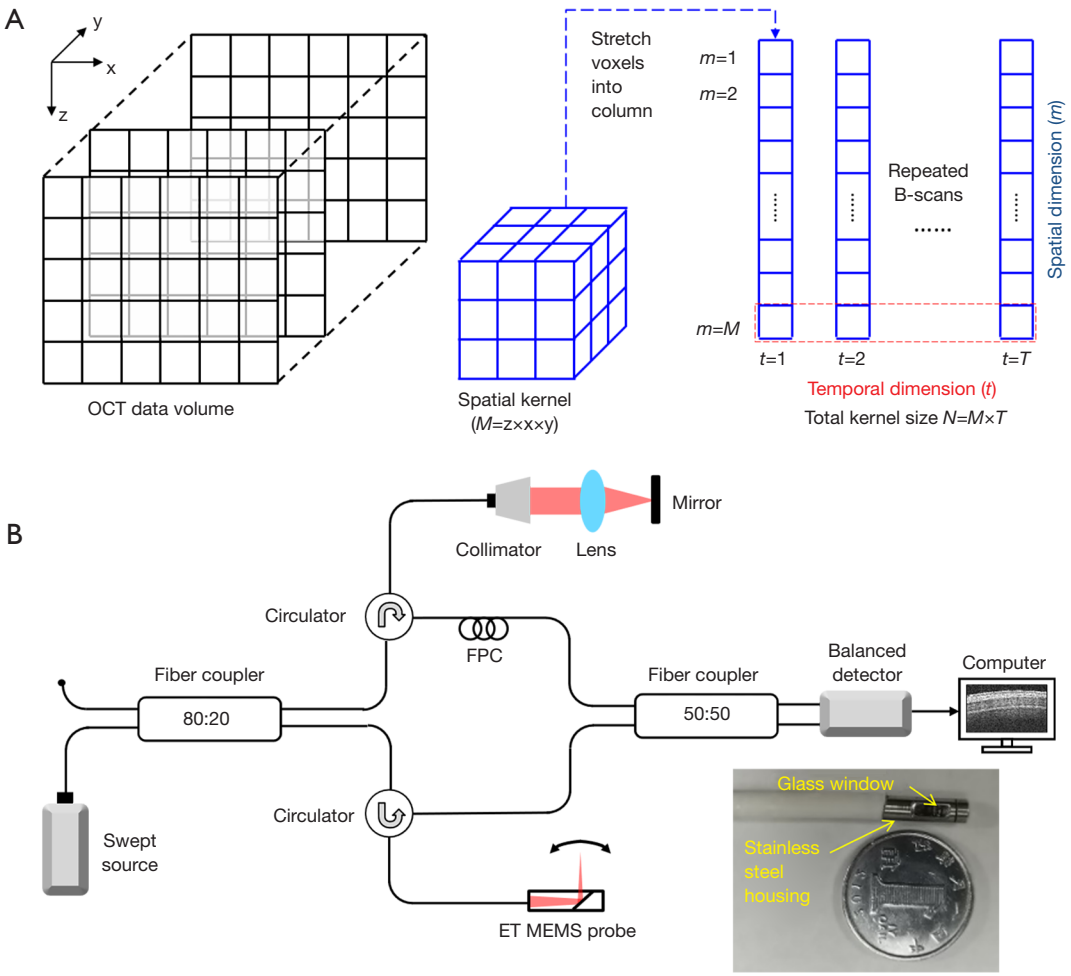

Figure 1 Schematics of the decorrelation calculation and the endoscopic SS-OCT system. (A) A spatial kernel (the blue volume) containing M voxels was extracted from the OCT volume data (the black volume). Decorrelation was calculated to evaluate the dissimilarity between T repeated scans with a total kernel size of $N=M\times T$. (B) SS-OCTA system with an endoscopic MEMS-based catheter as the sample arm. The insert shows a picture of the probe. SS-OCT, swept source optical coherence tomography; OCTA, OCT angiography; ET MEMS, electrothermal microelectromechanical system; FPC, fiber polarization controller.

the asymptotic amplitude decorrelation $\bar{D}$ is given by:

$$\bar{D}\to 1-\frac{E\left[x_0(m,t)x_0(m,t+1)\right]}{I}=1-\frac{E^2(x_0)}{E\left(x_0^2\right)}=1-iSNR\cdot E^2(x_0),\quad a.s. \quad [5]$$

where $E[\cdot]$ denotes expectation and a.s. means convergence with probability one. Particularly, in static regions, the mean value of decorrelation $\overline{D_{st}}$ could be further simplified, based on Eqs. [2,3]:

$$\begin{aligned}\overline{D_{st}}&\to 1-iSNR\cdot\int_0^{+\infty}\left[\int_0^{+\infty}p_{X_0|A_0=a_0}(x_0)x_0dx_0\right]^2p_{A_0}(a_0)da_0\\&=1-\frac{\pi iSNR^2}{2(1-iSNR)}\int_0^{+\infty}\left[L_{0.5}\left(-a_0^2\right)\right]^2e^{-\frac{iSNR}{1-iSNR}a_0^2}a_0da_0,\quad a.s.\end{aligned} \quad [6]$$

where $L_{0.5}$ is a Laguerre polynomial. Furthermore, the decorrelation in the totally dynamic regions where OCT signals are totally uncorrelated between repeated B-scans should be the same as that in background noise regions. Accordingly, the asymptotic decorrelation $\overline{D_{dy}}$ in totally dynamic regions can be easily obtained by setting $iSNR\to 1$ in Eq. [6] (see details in Appendix 1):

$$\overline{D_{dy}}\to 1-\frac{\pi}{4}\approx 0.22,\quad a.s. \quad [7]$$

Variance of IDa distribution

In addition, the IDa relation has a kernel-dependent variance. To facilitate derivation, the amplitude

decorrelation of OCT signals obtained from the same voxel and 2 time points was analyzed:

$$D = 1 - \frac{2x_0(t)x_0(t+1)}{x_0^2(t) + x_0^2(t+1)} \quad [8]$$

For specific SNR level SNR^*, i.e., $x_0^2(t) + x_0^2(t+1) = 2SNR^*$ or $x_0(t+1) = \sqrt{2SNR^* - x_0^2(t)}$, the decorrelation value $D(x_0(t))$ with respect to $x_0(t)$ is equal to:

$$D\left(x_0(t)\right) = 1 - iSNR^* x_0(t)\sqrt{2SNR^* - x_0^2(t)} \quad [9]$$

The PDF of the decorrelation for OCT signals in the static region satisfies the following equation (see details in Appendix 1):

$$p_{D(x_0(t))|SNR^*}\left(x_0(t)\right) = \int_0^1 p_{isnr}(iSNR)\,diSNR \int_0^{+\infty} p_{A_0}(a_0)\,da_0$$
$$\mathrm{p}_{X_0|A_0=a_0}\left(\mathrm{x}_0(\mathrm{t})\right)\mathrm{p}_{X_0|A_0=a_0}\left(\mathrm{x}_0(\mathrm{t}+1)\right)\sqrt{1+\left(\frac{\partial x_0(t+1)}{\partial x_0(t)}\right)^2} \quad [10]$$

with $x_0(t)$ ranging from 0 to $\sqrt{2SNR^*}$. $p_{isnr}(iSNR)$ is the PDF of iSNR of OCT signals. According to the exponential attenuation model of light intensity (36), the PDF of iSNR satisfies the following equation:

$$p_{isnr}(iSNR) \propto \frac{dz}{d\left(\frac{1}{I(z)}\right)} \propto I(z) \propto \frac{1}{iSNR} \quad [11]$$

where $I(z)$ is the signal intensity of the incident light beam at the depth of z.

According to Eqs. [10,11], the standard deviation (std) of decorrelation calculated by Eq. [8] satisfies the following:

$$\sigma_{st0}^2 = \int_0^{\sqrt{2SNR^*}} \left\{D\left(x_0(t)\right) - E\left[D\left(x_0(t)\right)\right]\right\}^2 \cdot p_{D(x_0(t))|SNR^*}\left(x_0(t)\right)\cdot dx_0(t) \quad [12]$$

where σ_{st0} is the decorrelation std with a temporal kernel size T=2, and $E\left[D\left(x_0(t)\right)\right] = \int_0^{\sqrt{2SNR^*}} D\left(x_0(t)\right)\cdot p_{D(x_0(t))|SNR^*}\left(x_0(t)\right)\cdot dx_0(t)$ is the decorrelation expectation. Furthermore, it should be noticed that $E[D(x_0(t))]$ is not equal to the result of Eq. [6] because decorrelation is not a non-biased variable here. Furthermore, assuming the samples from spatial and temporal dimensions are independent from each other, the variance of the IDa distribution is inversely proportional to the total spatio-temporal kernel size $N=M\cdot T$. In that case, the decorrelation std of static OCT signals is as follows:

$$\sigma_{st} = \sqrt{\frac{2}{N}}\sigma_{st0} \quad [13]$$

IDa-OCTA algorithm

To suppress the random noise-induced decorrelation artifacts, an SNR-adaptive IDa-OCTA algorithm was developed based on the derived asymptotic IDa relation and its distribution variance. In the proposed algorithm, the distribution area of static and noise voxels in the IDa space was predefined with the asymptote relation $\overline{D_{st}}$ (Eq. [6]) and an additional $3\sigma_{st}$ range (Eq. [13]). Accordingly, the distribution boundary can be described with a classification line D_c:

$$D_c(iSNR) = \overline{D_{st}} + 3\sigma_{st} = \overline{D_{st}} + 3\sqrt{\frac{2}{N}}\sigma_{st0} \quad [14]$$

The classification line is a function of iSNR and divides the IDa space into 2 parts: (I) dynamic ($D>D_c$) and (II) static/noise ($D\leq D_c$). The mathematical expression of the classifier infers that a larger kernel size improves the performance of the classifier by decreasing the distribution std in the IDa space. However, enlarging the spatial kernel degrades the spatial resolution, while enlarging the temporal kernel increases the imaging time (37). Therefore, an appropriate kernel size should be selected by trading off between the classification accuracy, spatial resolution, and imaging time. The implementation of the IDa-OCTA classifier can be divided into the following steps. First, all voxels were projected from ZXY space into IDa space, the dynamic voxels were labelled as 1 and others were labelled as 0. Second, an IDa mask was generated by reprojecting the labeled voxels from IDa space into ZXY space. Finally, the IDa-OCTA angiograms were generated by multiplying the original decorrelation map by the IDa mask. The framework of the IDa-OCTA algorithm is summarized in the pseudo-code shown in *Table 1*.

System setup

Figure 1B shows the schematic diagram of the proposed ET MEMS-based endoscopic IDa-OCTA system. The OCTA light source is a MEMS-tunable vertical cavity surface-emitting laser (VCSEL; Thorlabs, Newton, NJ, USA; SL131090). The laser can sweep at a rate of 100 kHz over a broad spectral bandwidth of approximately 100 nm with the center wavelength of 1,300 nm, providing an experimental axial resolution of approximately 16 μm and an imaging range of approximately 11 mm in the air. The output light from the laser source was first fiber-coupled into an interferometer, where the light was split by an 80:20 fiber coupler into a sample arm and a reference arm. The sample arm was

Table 1 Framework of the IDa-OCTA algorithm

Input:

(I) Spatio-temporal kernel size n_z, n_x, n_y and T;

(II) OCT amplitude data $A(z, x, y, t)$ with a size of N_z, N_x, N_y and T in the z, x, y and t dimensions, respectively;

(III) The global noise level σ_n^2 calculated in advance by taking the average of the signal intensity in the air region and the bottom noise region

Output: 3D IDa-OCTA angiograms

1: for all spatial windows with a size of $n_z \times n_x \times n_y$ do

/* Project voxel from ZXY space into IDa space */

2: Calculate local decorrelation $D(z, x, y)$ and intensity $I(z, x, y)$;

3: $iSNR(z,x,y) \leftarrow \frac{s^2}{I(z,x,y)}$;

/* Perform digital etch based on the classification line and reproject the labeled voxels from IDa space into ZXY space */

4: Calculate the classification line $D_C(z, x, y)$ based on Eq. [14] with $iSNR(z, x, y)$;

5: if $D(z, x, y) > D_C(z, x, y)$ then

6: $IDa_{mask}(z, x, y) \leftarrow 1$;

7: else

8: $IDa_{mask}(z, x, y) \leftarrow 0$;

9: end if;

10: end for;

11: Generate 3D IDa-OCTA angiograms by multiplying decorrelation $D(z, x, y)$ and $IDa_{mask}(z, x, y)$

OCT, optical coherence tomography; IDa, inverse signal noise ratio and amplitude decorrelation; IDa-OCTA, IDa-OCT angiography.

terminated in an ET MEMS-based probe (Wio Tech, Wuxi, China; MOCT-SV25) which allowed light to be transmitted to and collected from the sample, offering an experimental lateral resolution of approximately 31 μm. The probe is 3.5 mm in diameter and encapsulates all material in a stainless-steel housing with a glass window (2.5 mm × 5.5 mm) for light to transmit. The light that backscattered from the sample was recombined with the light reflected from the reference mirror, and then the interference signal was detected by a balanced detector (Newport Corp., Irvine, CA, USA; 1817-FC).

In the ET MEMS probe, both the fast and slow-axis scanning were driven with triangular waveforms varying from 0 to 5 V, which were linearly related to the scanning angle of the MEMS mirror. Due to the frequency response limitation of the MEMS mirror (38), a fast-axis scan frequency of 50 Hz (up to 200 Hz) was adopted in this study to achieve a large FOV of 2.3 mm × 2.3 mm. A stepwise raster scanning protocol (z-x-y) was used for volumetric imaging, with 1,000 A-lines per B-scan (fast-scan, x direction) and 1,000 B-scans repeated 5 times at 200 tomographic positions per volume (slow-scan, y direction). This study was conducted in accordance with the Declaration of Helsinki (as revised in 2013), approved by Ethics Committee of Zhejiang University (No. IRB-2021-461), and informed consent was provided by participants before imaging.

Correction of nonlinear distortion and bulk motion

Due to the ringing of the mirror plate at the turning points of the triangular waveforms, the ET MEMS response is nonlinear at both the beginning and the end of each B-frame (39), and the scope of corresponding regions is determined by the scan rate of the MEMS mirror (40). The nonlinear distortion was corrected by resampling B-frames at a rate proportional to the actual transversal scanning velocity v_x, which was estimated based on the speckle intensity cross-

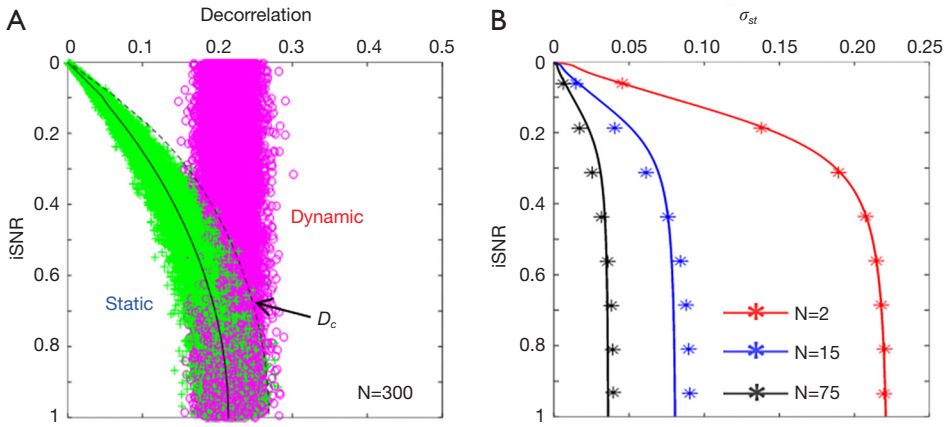

Figure 2 IDa asymptotic relation, distribution variance, and the classification line. (A) Scatter plots of static (green crosses) and dynamic (pink circles) signals in the IDa space. Amplitude decorrelation was calculated with a total kernel size N of 300. The black solid line denotes the theoretical asymptotic relation (Eq. [6]) and the black dashed line is the theoretical classification boundary D_c (Eq. [14]). (B) Plots of the distribution std of static signals σ_{st} over iSNR for kernel sizes of N=2 (red), N=15 (blue) and N=75 (black). The scatters are the results of numerical simulation, and the solid curves correspond to theoretical derivation Eq. [13]. IDa, inverse signal noise ratio and amplitude decorrelation; iSNR, inverse signal-to-noise ratio; std, standard deviation.

correlation g between adjacent A-lines (19):

$$|v_x| = \frac{b}{\sqrt{-2/\ln(g-1)}} \quad [15]$$

where the parameter b is related to the transverse point spread function of the system and the time interval between adjacent A-lines and is a constant for a certain system setting. A large cross-correlation g value indicates an ultra-low scanning speed and a serious nonlinear effect, which should be down sampled at a larger ratio. The inter-frame bulk motion induced by inevitable heartbeat and breathing was further corrected with a cross-correlation-based registration algorithm prior to the IDa-OCTA processing (41).

Results

Numerical simulation was performed to validate the asymptotic IDa relation and the proposed classification line. In the simulation, OCT signals were generated based on Eq. [1] and the basic spatio-temporal distribution characteristics of static and dynamic signals (14). As shown in *Figure 2A*, both iSNR and amplitude decorrelation for static (green) and dynamic (pink) signals were computed with a spatio-temporal kernel size of 15×20 (M×T) and then projected into IDa space. The static signals were distributed around its theoretical asymptote (black solid line, Eq. [6]) and could be effectively removed by the classification line D_c (black dashed line, Eq. [14]), which demonstrates the correctness of the theoretical derivation. *Figure 2B* illustrates the theoretical (solid lines) and simulated (scatters) relation between the distribution std and iSNR for static signals with different total kernel sizes. The simulated results agreed well with the theoretical results with R^2=1.000 for N=2 (red), R^2=0.914 for N=15 (blue), and R^2=0.896 for N=75 (black).

The flow phantom experiment was performed to demonstrate the correction effect of the ET MEMS-induced nonlinear distortion and the validity of the proposed IDa-OCTA method. The flow phantom was composed of 2 parts: 1 was a solid gel mixed with low concentration milk to mimic static tissues, and the other part was a milk solution to mimic dynamic flow. The milk solution was isolated from the solid gel by capillary tubes with inner diameter of 0.3±0.1 mm. As shown in the structural cross-section *Figure 3A*, a total of 4 capillary tubes were embedded in the solid gel at different depths to simulate blood flow with different SNR (the lowest <10 dB), and the nonlinear distortion was apparent at the end of the transverse scan (see the bold arrow in the inset of *Figure 3A*). The distortion was well corrected with the cross-correlation method as indicated by the circular shape of the tube cross-section (see the bold arrow in *Figure 3A*). After registration, a static region with nonlinear distortion was selected (see the dashed red rectangle in *Figure 3A*) and the average decorrelation of the high SNR region (mean iSNR =0.2) was 0.012, which was

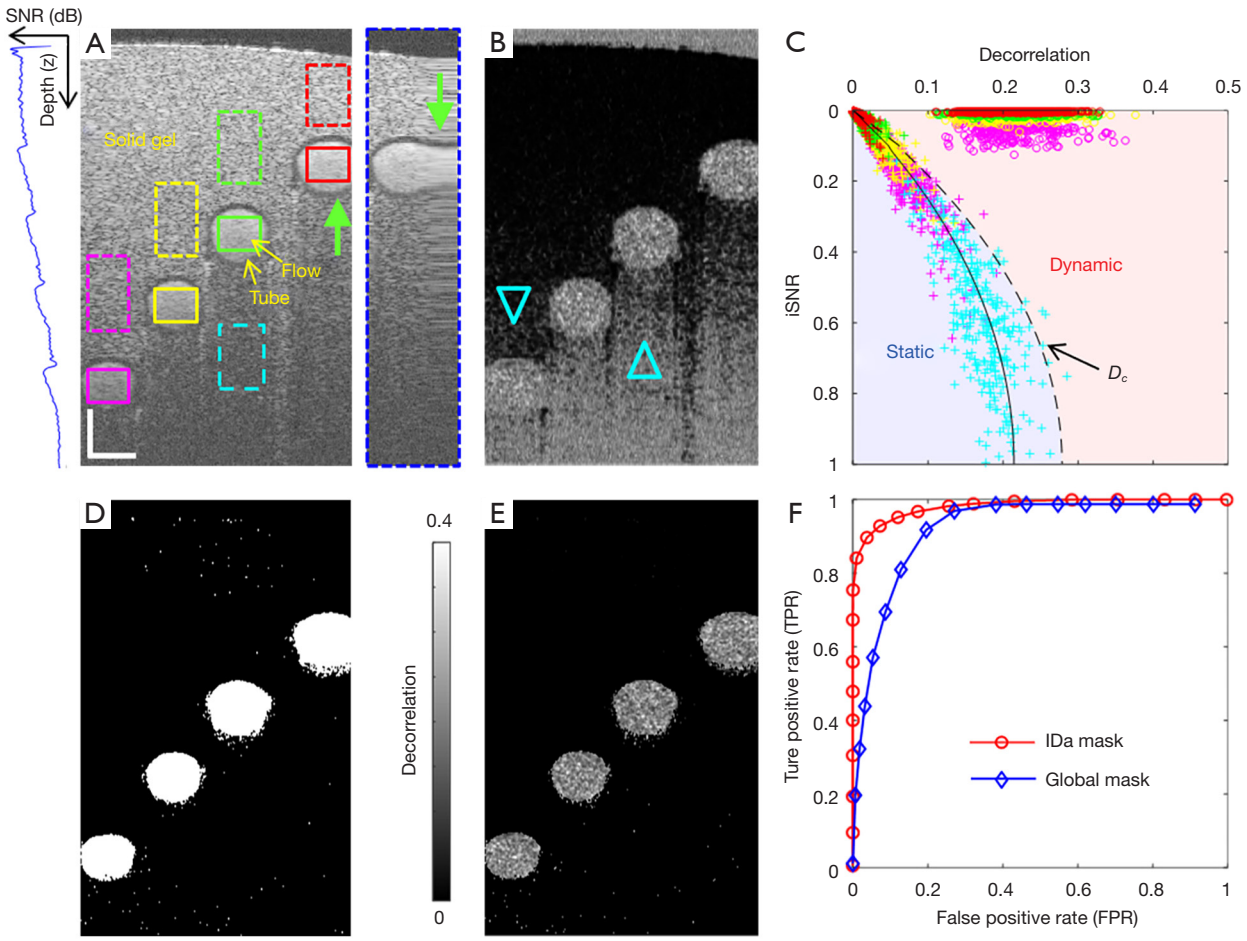

Figure 3 Validation of the correction effect of the ET MEMS-induced nonlinear distortion and the performance of the IDa-OCTA method through flow phantom experiment. (A) Structural cross-section of the flow phantom after distortion correction. Left inset is the averaged depth profile indicating the SNR decay. Right inset shows the nonlinear distortion part before correction. The bold arrows highlight the region of nonlinear distortion. The mean iSNR and SNR of the deepest flow region (the solid pink rectangle in A) were approximately 0.09 and 10 dB, respectively. (B) Cross-sectional decorrelation mapping. The static regions marked with cyan triangles present high decorrelation due to the dominant random noise (i.e., low SNR). (C) The predefined static and dynamic parts in IDa space are calculated according to Eq. [14] and the scatterplots of the static (dashed rectangles in A) and dynamic (solid rectangles in A) voxels in IDa space. The solid and dashed lines correspond to the theoretical asymptotic IDa relation determined by Eq. [6], and the classification line D_c determined by Eq. [14], respectively. (D) Cross-sectional IDa mask generated by digitally etching the IDa-defined static and noise components. (E) Cross-sectional IDa-OCTA angiogram achieved by overlying IDa mask (D) on decorrelation mapping (B). A large 4D spatio-temporal decorrelation kernel of 5 × 5 ×3 × 4 (z × x × y × t) was used for a convergent IDa asymptotic distribution. (F) Receiver-operating characteristic curve of the IDa masks with different multiples of std and the 2-step-3σ thresholding method. A fixed global intensity threshold (the mean noise level adds its triple std) and a sequence of global decorrelation thresholds were combined in the 2-step 3σ thresholding method to perform digital etch. Besides, a practical kernel of 5 × 3 × 1 × 5 (z × x × y × t) was adopted to compare the performance of the IDa mask and global mask. Scale bar =0.3 mm. ET MEMS, electrothermal microelectromechanical system; IDa, inverse signal noise ratio and amplitude decorrelation; IDa-OCTA, IDa-optical coherence tomography angiography; SNR, signal noise ratio; iSNR, inverse SNR; std, standard deviation.

similar to the results obtained by galvo scanner (0.016) (6), indicating the good inter-frame scanning stability of the MEMS scanner after registration. As shown in the decorrelation mapping in *Figure 3B*, generally, the dynamic flow presented a high decorrelation value, while that of static region was low. However, due to the influence of the additional random noise, deep static regions also presented high decorrelation values (i.e., noise-induced decorrelation artifacts) as highlighted by the cyan triangles in *Figure 3B*. According to the derived classification line D_c (see the dashed curve in *Figure 3C* determined by Eq. [14]), the IDa feature space can be separated into 2 parts: static and dynamic. The scatterplots of the static (the dashed rectangles in *Figure 3A*) and dynamic (the solid rectangles in *Figure 3A*) voxels were in good agreement with the predefined IDa space. After labelling the voxels above the line D_c as 1 and the others as 0 in IDa space, the digital etch created an IDa mask (see *Figure 3D*). Overlying the IDa mask onto the decorrelation mapping generated the resultant IDa-OCTA angiogram (see *Figure 3E*). To quantitatively evaluate the classification performance of IDa-OCTA, the true positive rate (TPR; 82.9%) and false positive rate (FPR; 0.7%) were calculated. The area under the receiver-operating characteristic (ROC) curve (see *Figure 3F*) of the IDa masks with different multiples of std was significantly larger than that of the 2-step-3σ thresholding method where a global intensity threshold (the mean noise level add its triple std) and a series of decorrelation thresholds were used in digital etch (42), indicating a superior performance of the IDa-OCTA classifier.

In human oral mucosa imaging, the probe was gently placed on the right buccal mucosa of a healthy female volunteer, and the side-viewing endoscopic IDa-OCTA enabled the visualization of mucosal vasculature inside the mouth. As illustrated by the 3D anatomical structure (*Figure 4A*), the buccal mucosa is divided into the epithelial (EP), lamina propria (LP), and underlying submucosa (SM) layers. The LP layer, which is a fibrous connective tissue layer consisting of a network of collagen and elastin fibers, is further divided into 2 sub-layers: papillary (pLP) and reticular (rLP) layers (43). The vascular plexus in the rLP layer provides a horizontal branching network of blood vessels from which ascending arterioles project into the pLP layer, forming capillary networks, and subsequently drain back into descending venules (44,45). The nonlinear distortion was also well corrected (see Figure 4B and its insert) in the *in vivo* imaging with the cross-correlation method. The pLP and rLP layers presented low and high OCT intensity in the structural cross-section (*Figure 4B*), based on which the interface of pLP-rLP layers was segmented, which was most likely due to the difference between delicate and thick collagen fibers. In cross-sectional decorrelation mapping (*Figure 4C*), the deep static tissue background also presented high decorrelation values due to the influence of the random noise. Under the guidance of the predefined classification line in IDa space (*Figure 4D*), an IDa flow mask was generated with a digital etch, and the resultant angiogram was generated by overlaying the flow mask onto the decorrelation mapping (*Figure 4E*). The cross-sectional IDa-OCTA angiogram (*Figure 4E*) shows superficial plexuses (SP), which reside within the LP, supplying nutrients and oxygen for capillary loops (CL) entering the connective tissue papillae. The EP and SM layers were roughly determined according to the depth location of the CL and SP (*Figure 4E*,*4F*). Depth-resolved vascular networks were visualized from the 3D IDa-OCTA image (*Figure 4G*,*4H*). The *en face* (x-y) angiogram of pLP presents concentrated and lengthy capillary loops which originate from the underlying vascular plexus in the LP. The LP plexus could be more clearly identified from the deeper reticular layer (rLP), as shown in *Figure 4H*. Regardless of the FOV and lateral resolution, our endoscopic IDa-OCTA achieved a similar performance in vascular imaging of oral mucosa to that of a bench-top OCTA reported in Wei's study (43). Furthermore, we noticed that tail artifacts were not obvious in mucosal imaging, which was because large vessels were located under capillaries, so superficial vessels did not significantly degrade the imaging quality of deeper vasculature. In future studies, such as tumor neovascularization imaging, the presented tail artifacts can be removed with projection-resolved algorithms if necessary (46).

Discussion

Although SS-OCT system is widely used in endoscopic imaging because of its advantages in sensitivity and imaging range (47,48), its phase is unstable, which reduces its popularity for use in OCTA motion contrast calculation. In this study, amplitude decorrelation was computed to evaluate the RBC motion. To suppress the noise-induced decorrelation artifacts, we mathematically derived the asymptotic IDa relation based on the MVTS model and the distribution variance based on probability analysis. Numerical simulation and flow phantom experiments were performed to demonstrate its validity. According to the derived asymptotic IDa relation, all dynamic and static

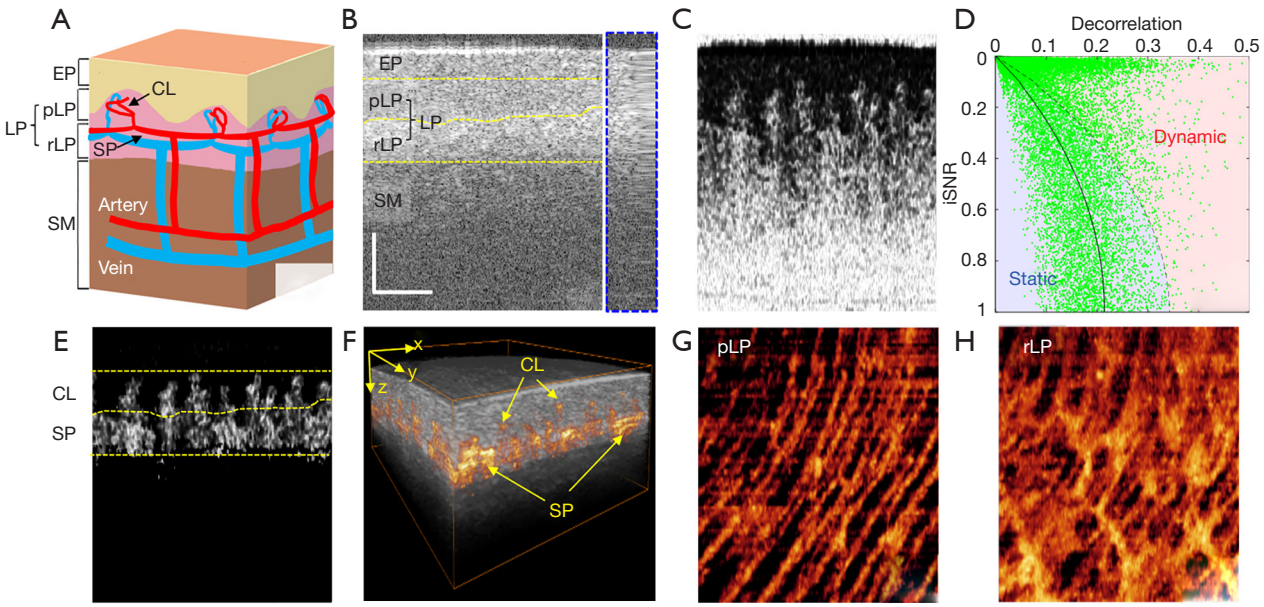

Figure 4 *In vivo* endoscopic IDa-OCTA imaging of the buccal mucosa of a healthy volunteer with side-viewing ET MEMS catheter. (A) 3D anatomy representation. Representative cross-sectional (x-z) (B) structure and (C) decorrelation mapping. Right inset of (B) shows the nonlinear distortion part before correction. (D) IDa space mapping of the cross-sectional data and the proposed classifier. (E) Cross-sectional IDa-OCTA angiogram. (F) Volume rendered representation of the fused OCT structure (gray) and IDa-OCTA vasculature (yellow) image dataset. *En face* (x-y) MIP angiograms (2 mm × 2.3 mm) of (G) pLP and (H) rLP layers, respectively. The pLP and rPL layers present dense superficial capillary loops and vascular plexus, respectively. A spatio-temporal decorrelation kernel of 5 × 3 × 1 × 5 (z × x × y × t) was used as a tradeoff between resolution and motion contrast. Scale bar = 0.5 mm. EP, epithelial; LP, lamina propria; pLP, papillary LP; rLP, reticular LP; SM, submucosa; CL, capillary loops; SP, superficial plexuses; OCT, optical coherence tomography; IDa-OCTA, inverse signal noise ratio and amplitude decorrelation OCT angiography; ET MEMS, electrothermal microelectromechanical system; MIP, maximum intensity projection.

signals with SNR >1 can be distinguished, provided that the kernel size N is sufficiently large. However, the kernel size is limited in practice, and with the decrease of kernel size, the distribution variance and overlapping region of signals in IDa space increase accordingly (refer to *Figure 2*), which limits the ability to extract flow signals in the low-SNR regions. Using the knowledge of the exact IDa distribution, the noisy blood flow signals can be further enhanced by combining the tube shape feature of the vessels as reported by Li *et al.* (49). The saturation limit of amplitude decorrelation was compressed to approximately 0.22, which is 1 in complex decorrelation (a decrease of 78%), and most likely due to the loss of the ultra-motion-sensitive phase information, (50). Accordingly, the amplitude decorrelation might have an inferior motion contrast compared to complex decorrelation (41,51). Therefore, we suggest using amplitude-based IDa-OCTA in the phase-instable system and complex-based ID-OCTA in the phase-stable system. In the future, a detailed performance comparison between the amplitude and complex decorrelation could be performed with a phase-stable spectral domain system.

The proposed IDa-OCTA algorithm has several advantages compared with existing methods. Rather than using learning methods to generate a classification map based on feature space, which depends on specific scanning protocol and phantom fabrication (15), the IDa classification line is universal. In contrast to the proposed regression method which can only obtain 2D binary vascular projection (16), 3D IDa-OCTA angiograms were obtained in our study. Furthermore, existing methods lack a clear relation of motion contrast to SNR, but the asymptotic IDa relation and its distribution variance were rigorously derived in this study. Furthermore, in our study, the simulated results agree well with the theoretical calculation, which differed from the variance analysis based on Cramer-Rao lower bound (CRLB), where the variance is not accurate

and serious outliers appear in the case of a practical and limited kernel size (52). In addition, by taking the advantage of accurate derivation, there is potential to further enhance the classification accuracy by dividing the IDa space more precisely and combining additional features (49). Although the IDa-OCTA algorithm was demonstrated with the ET MEMS in this study, it does not rely on a specific scanner, and can be readily used along with other scanning modalities (6,17-19,21-27).

Raster scan is widely used in the benchtop OCTA system that uses a galvo scanner (4-6). Compared with the spiral scanning pattern, the spatial sampling of sequential B-frames is the same in the raster pattern, which provides a stable and controllable time interval and minimizes the decorrelation noise in the tissue background. In this work, we demonstrated that ET MEMS can be used to achieve a distal raster scan. Although its FOV is limited compared with that of a rotary scanning probe, it is more convenient for doctors to inspect specific suspicious areas in real time. In addition to the tubular organs, it is also suitable for hollow organ imaging, such as the oral cavity, stomach, and bladder. Furthermore, in addition to the side-viewing demonstrated in this work, ET MEMS can also be used to achieve a forward-viewing raster scan with a cantilever, which can be used in image-guided biopsy and surgery (53). In the future, a dedicated spacer might be used between the imaged tissue and the probe head to suppress the bulk motion in OCTA imaging.

The probe we used had a 3.5 mm diameter and 16.7 mm rigid length; it could be easily inserted through therapeutic endoscopes with a 3.7 mm working channel, but was still too large to pass through commonly used esophagogastroduodenoscopy (EGD) endoscopes with a 2.8 mm working channel (54). Currently, the ET MEMS mirror chip is mounted on a 45° sloped ferrule, and the electrical connection is powered by a reliable wire bonding method, both of which increase the probe size. The probe size can be further reduced by replacing the current fabrication with a 45° titled MEMS mirror directly integrated on a silicon optical bench (SiOB), which provides both mechanical support and stable electrical connection. A compact probe with a 2.7 mm diameter and 15 mm rigid length has been reported for OCT structural imaging (55). In addition, the lateral resolution of the system was mainly determined by the spot radius focused by the cylindrical gradient-index (GRIN) lens. It can be optimized by increasing the gradient constant of the GRIN lens or the distance between single-mode fiber (SMF) and GRIN lens, although at the cost of decreasing working distance and FOV (56,57). The current 31 μm lateral resolution was chosen for a large FOV of 2 mm × 2.3 mm, which can be improved to 18 μm with a decreased FOV of 1.2 mm × 1.38 mm for visualization of more detailed vascular features (57). The vascular patterns change as the tumors invade from epithelium to submucosa (1). The depth-resolved vasculature revealed by endo-OCTA might offer a precise estimation of the tumor invasion depth, which is of great value in clinical diagnosis.

In this work, we proposed an endoscopic SNR-adaptive SS-OCTA with an ET MEMS raster scan. To suppress the system noise-induced decorrelation artifacts, the IDa asymptotic relation and its distribution variance were theoretically derived and then validated through numerical simulation and flow phantom experiments. Accordingly, we defined an SNR-adaptive classification line in IDa space to generate an IDa flow mask in ZXY space. An SNR-adaptive IDa-OCTA was achieved by combining the IDa mask and the decorrelation contrast. A distal stepwise raster scan was achieved with a low-voltage ET MEMS-based catheter for endoscopic imaging, and the repeated B-scans at each step suppressed the decorrelation noise induced by spatial mismatch between paired scans. The endoscopic IDa-OCTA imaging was demonstrated with *in vivo* human buccal mucosa imaging, which enabled the visualization of subsurface structure and vasculature in a rapid and depth-resolved manner. These unique features of the endoscopic IDa-OCTA offer potential to improve the early diagnostic capability for internal organs.

Acknowledgments

Funding: This work was supported by the National Natural Science Foundation of China (No. 62075189), Zhejiang Provincial Natural Science Foundation of China (No. LR19F050002), Zhejiang Lab (No. 2018EB0ZX01), Hebei Key Laboratory of Micro-Nano Precision Optical Sensing and Measurement Technology (No. NEUQ202104), and MOE Frontier Science Center for Brain Science & Brain-Machine Integration, Zhejiang University.

Footnote

Reporting Checklist: The authors have completed the MDAR checklist. Available at https://qims.amegroups.com/article/view/10.21037/qims-21-1056/rc

Conflicts of Interest: All authors have completed the ICMJE uniform disclosure form (available at https://qims.amegroups.com/article/view/10.21037/qims-21-1056/coif). PL reports that this work was supported by the National Natural Science Foundation of China (No. 62075189), Zhejiang Provincial Natural Science Foundation of China (No. LR19F050002), Zhejiang Lab (No. 2018EB0ZX01), Hebei Key Laboratory of Micro-Nano Precision Optical Sensing and Measurement Technology (No. NEUQ202104), and MOE Frontier Science Center for Brain Science & Brain-Machine Integration, Zhejiang University. PL works in the Zhejiang University and discloses intellectual property owned by Zhejiang University. The other authors have no conflicts of interest to declare.

Ethical Statement: The authors are accountable for all aspects of the work in ensuring that questions related to the accuracy or integrity of any part of the work are appropriately investigated and resolved. This study was conducted in accordance with the Declaration of Helsinki (as revised in 2013). This study was approved by Ethics Committee of Zhejiang University (No.: IRB-2021-461), and informed consent was provided by participants before imaging.

References

1. Kumagai Y, Toi M, Inoue H. Dynamism of tumour vasculature in the early phase of cancer progression: outcomes from oesophageal cancer research. Lancet Oncol 2002;3:604-10.
2. Sharma P, Bansal A, Mathur S, Wani S, Cherian R, McGregor D, Higbee A, Hall S, Weston A. The utility of a novel narrow band imaging endoscopy system in patients with Barrett's esophagus. Gastrointest Endosc 2006;64:167-75.
3. Wallace M, Lauwers GY, Chen Y, Dekker E, Fockens P, Sharma P, Meining A. Miami classification for probe-based confocal laser endomicroscopy. Endoscopy 2011;43:882-91.
4. Wang RK, Jacques SL, Ma Z, Hurst S, Hanson SR, Gruber A. Three dimensional optical angiography. Opt Express 2007;15:4083-97.
5. Jia Y, Tan O, Tokayer J, Potsaid B, Wang Y, Liu JJ, Kraus MF, Subhash H, Fujimoto JG, Hornegger J, Huang D. Split-spectrum amplitude-decorrelation angiography with optical coherence tomography. Opt Express 2012;20:4710-25.
6. Huang L, Fu Y, Chen R, Yang S, Qiu H, Wu X, Zhao S, Gu Y, Li P. SNR-Adaptive OCT Angiography Enabled by Statistical Characterization of Intensity and Decorrelation With Multi-Variate Time Series Model. IEEE Trans Med Imaging 2019;38:2695-704.
7. Skalet AH, Li Y, Lu CD, Jia Y, Lee B, Husvogt L, Maier A, Fujimoto JG, Thomas CR Jr, Huang D. Optical Coherence Tomography Angiography Characteristics of Iris Melanocytic Tumors. Ophthalmology 2017;124:197-204.
8. Lu Y, Wang JC, Zeng R, Nagata T, Katz R, Mukai S, Miller JB. Detection of retinal microvascular changes in von Hippel-Lindau disease using optical coherence tomography angiography. PLoS One 2020;15:e0229213.
9. Custo Greig EP, Duker JS. Retinal hemangioblastoma vascular detail elucidated on swept source optical coherence tomography angiography. Am J Ophthalmol Case Rep 2021;21:101005.
10. Tsai TH, Ahsen OO, Lee HC, Liang K, Figueiredo M, Tao YK, Giacomelli MG, Potsaid BM, Jayaraman V, Huang Q, Cable AE, Fujimoto JG, Mashimo H. Endoscopic optical coherence angiography enables 3-dimensional visualization of subsurface microvasculature. Gastroenterology 2014;147:1219-21.
11. Lee HC, Ahsen OO, Liang K, Wang Z, Figueiredo M, Giacomelli MG, Potsaid B, Huang Q, Mashimo H, Fujimoto JG. Endoscopic optical coherence tomography angiography microvascular features associated with dysplasia in Barrett's esophagus (with video). Gastrointest Endosc 2017;86:476-484.e3.
12. Chen CL, Wang RK. Optical coherence tomography based angiography Invited. Biomed Opt Express 2017;8:1056-82.
13. Enfield J, Jonathan E, Leahy M. In vivo imaging of the microcirculation of the volar forearm using correlation mapping optical coherence tomography (cmOCT). Biomed Opt Express 2011;2:1184-93.
14. Cheng Y, Guo L, Pan C, Lu T, Hong T, Ding Z, Li P. Statistical analysis of motion contrast in optical coherence tomography angiography. J Biomed Opt 2015;20:116004.
15. Zhang A, Wang RK. Feature space optical coherence

tomography based micro-angiography. Biomed Opt Express 2015;6:1919-28.
16. Gao SS, Jia Y, Liu L, Zhang M, Takusagawa HL, Morrison JC, Huang D. Compensation for Reflectance Variation in Vessel Density Quantification by Optical Coherence Tomography Angiography. Invest Ophthalmol Vis Sci 2016;57:4485-92.
17. Yun SH, Tearney GJ, Vakoc BJ, Shishkov M, Oh WY, Desjardins AE, Suter MJ, Chan RC, Evans JA, Jang IK, Nishioka NS, de Boer JF, Bouma BE. Comprehensive volumetric optical microscopy in vivo. Nat Med 2006;12:1429-33.
18. Adler DC, Chen Y, Huber R, Schmitt J, Connolly J, Fujimoto JG. Three-dimensional endomicroscopy using optical coherence tomography. Nature Photonics 2007;1:709-16.
19. Uribe-Patarroyo N, Bouma BE. Rotational distortion correction in endoscopic optical coherence tomography based on speckle decorrelation. Opt Lett 2015;40:5518-21.
20. Gora MJ, Suter MJ, Tearney GJ, Li X. Endoscopic optical coherence tomography: technologies and clinical applications Invited. Biomed Opt Express 2017;8:2405-44.
21. Li J, de Groot M, Helderman F, Mo J, Daniels JM, Grünberg K, Sutedja TG, de Boer JF. High speed miniature motorized endoscopic probe for optical frequency domain imaging. Opt Express 2012;20:24132-8.
22. Liang K, Traverso G, Lee HC, Ahsen OO, Wang Z, Potsaid B, Giacomelli M, Jayaraman V, Barman R, Cable A, Mashimo H, Langer R, Fujimoto JG. Ultrahigh speed en face OCT capsule for endoscopic imaging. Biomed Opt Express 2015;6:1146-63.
23. Liang K, Wang Z, Ahsen OO, Lee HC, Potsaid BM, Jayaraman V, Cable A, Mashimo H, Li X, Fujimoto JG. Cycloid scanning for wide field optical coherence tomography endomicroscopy and angiography in vivo. Optica 2018;5:36-43.
24. Liang K, Ahsen OO, Wang Z, Lee HC, Liang W, Potsaid BM, Tsai TH, Giacomelli MG, Jayaraman V, Mashimo H, Li X, Fujimoto JG. Endoscopic forward-viewing optical coherence tomography and angiography with MHz swept source. Opt Lett 2017;42:3193-6.
25. Wurster LM, Shah RN, Placzek F, Kretschmer S, Niederleithner M, Ginner L, Ensher J, Minneman MP, Hoover EE, Zappe H, Drexler W, Leitgeb RA, Ataman Ç. Endoscopic optical coherence tomography angiography using a forward imaging piezo scanner probe. J Biophotonics 2019;12:e201800382.
26. Kim KH, Park BH, Maguluri GN, Lee TW, Rogomentich FJ, Bancu MG, Bouma BE, de Boer JF, Bernstein JJ. Two-axis magnetically-driven MEMS scanning catheter for endoscopic high-speed optical coherence tomography. Opt Express 2007;15:18130-40.
27. Jung W, McCormick DT, Zhang J, Wang L, Tien NC, Chen Z. Three-dimensional endoscopic optical coherence tomography by use of a two-axis microelectromechanical scanning mirror. Appl Phys Lett 2006;88:163901.
28. Liu L, Wu L, Sun J, Lin E, Xie H. Miniature endoscopic optical coherence tomography probe employing a two-axis microelectromechanical scanning mirror with through-silicon vias. J Biomed Opt 2011;16:026006.
29. Samuelson SR, Wu L, Sun J, Choe SW, Sorg BS, Xie H. A 2.8-mm Imaging Probe Based On a High-Fill-Factor MEMS Mirror and Wire-Bonding-Free Packaging for Endoscopic Optical Coherence Tomography. J Microelectromech Syst 2012;21:1291-302.
30. Choi WJ, Reif R, Yousefi S, Wang RK. Improved microcirculation imaging of human skin in vivo using optical microangiography with a correlation mapping mask. J Biomed Opt 2014;19:36010.
31. Braaf B, Donner S, Nam AS, Bouma BE, Vakoc BJ. Complex differential variance angiography with noise-bias correction for optical coherence tomography of the retina. Biomed Opt Express 2018;9:486-506.
32. Makita S, Kurokawa K, Hong YJ, Miura M, Yasuno Y. Noise-immune complex correlation for optical coherence angiography based on standard and Jones matrix optical coherence tomography. Biomed Opt Express 2016;7:1525-48.
33. Dubose TB, Cunefare D, Cole E, Milanfar P, Izatt JA, Farsiu S. Statistical Models of Signal and Noise and Fundamental Limits of Segmentation Accuracy in Retinal Optical Coherence Tomography. IEEE Trans Med Imaging 2018;37:1978-88.
34. Motaghiannezam R, Fraser S. Logarithmic intensity and speckle-based motion contrast methods for human retinal vasculature visualization using swept source optical coherence tomography. Biomed Opt Express 2012;3:503-21.
35. Cavazoscadena R. The Asymptotic Distribution of Sample Autocorrelations for a Class of Linear Filters. J Multivar Anal 1994;48:249-74.
36. Vermeer KA, Mo J, Weda JJ, Lemij HG, de Boer JF. Depth-resolved model-based reconstruction of attenuation coefficients in optical coherence tomography. Biomed Opt Express 2013;5:322-37.
37. Li H, Liu K, Yao L, Deng X, Zhang Z, Li P. ID-OCTA:

OCT angiography based on inverse SNR and decorrelation features. J Innov Opt Health Sci 2021;14:2130001.
38. Sun J, Guo S, Wu L, Liu L, Choe SW, Sorg BS, Xie H. 3D in vivo optical coherence tomography based on a low-voltage, large-scan-range 2D MEMS mirror. Opt Express 2010;18:12065-75.
39. Wang D, Fu L, Wang X, Gong Z, Samuelson S, Duan C, Jia H, Ma JS, Xie H. Endoscopic swept-source optical coherence tomography based on a two-axis microelectromechanical system mirror. J Biomed Opt 2013;18:86005.
40. Lu C, Xiong K, Ma Y, Zhang W, Cheng Z, Yang S. Electrothermal-MEMS-induced nonlinear distortion correction in photoacoustic laparoscopy. Opt Express 2020;28:15300-13.
41. Guo L, Li P, Pan C, Liao R, Cheng Y, Hu W, Chen Z, Ding Z, Li P. Improved motion contrast and processing efficiency in OCT angiography using complex-correlation algorithm. J Opt 2015;18:025301.
42. Zhang Y, Li H, Cao T, Chen R, Qiu H, Gu Y, Li P. Automatic 3D adaptive vessel segmentation based on linear relationship between intensity and complex-decorrelation in optical coherence tomography angiography. Quant Imaging Med Surg 2021;11:895-906.
43. Wei W, Choi WJ, Wang RK. Microvascular imaging and monitoring of human oral cavity lesions in vivo by swept-source OCT-based angiography. Lasers Med Sci 2018;33:123-34.
44. Braverman IM. The cutaneous microcirculation: ultrastructure and microanatomical organization. Microcirculation 1997;4:329-40.
45. Wurster LM, Kretschmer S, Jäger J, Placzek F, Ginner L, Drexler W, Ataman Ç, Leitgeb RA, Zappe H. Comparison of optical coherence tomography angiography and narrow-band imaging using a bimodal endoscope. J Biomed Opt 2019;25:1-5.
46. Zhang M, Hwang TS, Campbell JP, Bailey ST, Wilson DJ, Huang D, Jia Y. Projection-resolved optical coherence tomographic angiography. Biomed Opt Express 2016;7:816-28.
47. Tearney GJ, Brezinski ME, Bouma BE, Boppart SA, Pitris C, Southern JF, Fujimoto JG. In vivo endoscopic optical biopsy with optical coherence tomography. Science 1997;276:2037-9.
48. Suter MJ, Vakoc BJ, Yachimski PS, Shishkov M, Lauwers GY, Mino-Kenudson M, Bouma BE, Nishioka NS, Tearney GJ. Comprehensive microscopy of the esophagus in human patients with optical frequency domain imaging. Gastrointest Endosc 2008;68:745-53.
49. Li H, Liu K, Cao T, Yao L, Zhang Z, Deng X, Du C, Li P. High performance OCTA enabled by combining features of shape, intensity, and complex decorrelation. Opt Lett 2021;46:368-71.
50. Chen R, Yao L, Liu K, Cao T, Li H, Li P. Improvement of Decorrelation-Based OCT Angiography by an Adaptive Spatial-Temporal Kernel in Monitoring Stimulus-Evoked Hemodynamic Responses. IEEE Trans Med Imaging 2020;39:4286-96.
51. Xu J, Song S, Li Y, Wang RK. Complex-based OCT angiography algorithm recovers microvascular information better than amplitude- or phase-based algorithms in phase-stable systems. Phys Med Biol 2017;63:015023.
52. Gräfe MGO, Nadiarnykh O, De Boer JF. Optical coherence tomography velocimetry based on decorrelation estimation of phasor pair ratios (DEPPAIR). Biomed Opt Express 2019;10:5470-85.
53. Park HC, Zhang X, Yuan W, Zhou L, Xie H, Li X. Ultralow-voltage electrothermal MEMS based fiber-optic scanning probe for forward-viewing endoscopic OCT. Opt Lett 2019;44:2232-5.
54. Tsai TH, Lee HC, Ahsen OO, Liang K, Giacomelli MG, Potsaid BM, Tao YK, Jayaraman V, Figueiredo M, Huang Q, Cable AE, Fujimoto J, Mashimo H. Ultrahigh speed endoscopic optical coherence tomography for gastroenterology. Biomed Opt Express 2014;5:4387-404.
55. Duan C, Tanguy Q, Pozzi A, Xie H. Optical coherence tomography endoscopic probe based on a tilted MEMS mirror. Biomed Opt Express 2016;7:3345-54.
56. Jung W, Benalcazar W, Ahmad A, Sharma U, Tu H, Boppart SA. Numerical analysis of gradient index lens-based optical coherence tomography imaging probes. J Biomed Opt 2010;15:066027.
57. Duan C, Sun J, Samuelson S, Xie H. Probe alignment and design issues of microelectromechanical system based optical coherence tomography endoscopic imaging. Appl Opt 2013;52:6589-98.

Cite this article as: Yao L, Li H, Liu K, Zhang Z, Li P. Endoscopic optical coherence tomography angiography using inverse SNR-amplitude decorrelation features and electrothermal micro-electro-mechanical system raster scan. Quant Imaging Med Surg 2022;12(6):3078-3091. doi: 10.21037/qims-21-1056

Appendix 1

Derivation of Eq. [2]

The probability density function (PDF) $p_{|\tilde{A}|}\left(\left|\tilde{A}\right|\right)$ of the amplitude component of noiseless OCT signal $\left|\tilde{A}\right|$ follows the Rayleigh distribution (14):

$$p_{|\tilde{A}|}\left(\left|\tilde{A}\right|\right)=\frac{2\left|\tilde{A}\right|}{v^2}exp\left(-\frac{\left|\tilde{A}\right|^2}{v^2}\right), \quad [S1]$$

According to the definition, $a_0=\frac{\left|\tilde{A}\right|}{s}$ and $iSNR=\frac{s^2}{s^2+v^2}$, the PDF of a_0 can be expressed in terms of a_0 and $iSNR$:

$$p_{A_0}\left(a_0\right)=\frac{2iSNR\cdot a_0}{1-iSNR}e^{-\frac{iSNR}{1-iSNR}a_0^2}, \quad [S2]$$

Derivation of Eq. [3]

For signal in static region, in the temporal dimension, the resultant OCT signal $\tilde{X}$ is the sum of the constant phasor $\tilde{A}$ and the white Gaussian noise $\tilde{n}$. We assume the direction of the constant phasor as the real-axis for simplicity. The joint PDF $p_{\tilde{X}}\left(x,y\right)$ for the real and imaginary part of $\tilde{X}$ satisfies (14,34):

$$p_{\tilde{X}}\left(x,y\right)=\frac{1}{\pi s^2}exp\left[-\frac{\left(x-\left|\tilde{A}\right|\right)^2+y^2}{s^2}\right], \quad [S3]$$

where x and y are defined as the real and imaginary part of $\tilde{X}$. By transforming Eq. [S3] into the polar coordinate, the PDF $p_{\tilde{X}}\left(\left|\tilde{X}\right|,\theta\right)$ of $\tilde{X}$ can be expressed in terms of the amplitude $\left|\tilde{X}\right|$ and angle θ of $\tilde{X}$:

$$p_{\tilde{X}}\left(\left|\tilde{X}\right|,\theta\right)=\frac{1}{\pi s^2}exp\left[-\frac{\left|\tilde{X}\right|^2+\left|\tilde{A}\right|^2-2\left|\tilde{X}\right|\left|\tilde{A}\right|\cos\theta}{s^2}\right]. \quad [S4]$$

The marginal PDF $p_{|\tilde{X}|}\left(\left|\tilde{X}\right|\right)$ of the amplitude $\left|\tilde{X}\right|$ can be obtained by integrating over θ:

$$p_{|\tilde{X}|}\left(\left|\tilde{X}\right|\right)=\int_{-\pi}^{\pi}p_{\tilde{X}}\left(\left|\tilde{X}\right|,\theta\right)d\theta$$

$$=\frac{1}{\pi s^2}exp\left(-\frac{\left|\tilde{X}\right|^2+\left|\tilde{A}\right|^2}{s^2}\right)\int_{-\pi}^{\pi}exp\left(\frac{2\left|\tilde{X}\right|\left|\tilde{A}\right|\cos\theta}{s^2}\right)d\theta=\frac{2}{s^2}exp\left(-\frac{\left|\tilde{X}\right|^2+\left|\tilde{A}\right|^2}{s^2}\right)I_0\left(\frac{2\left|\tilde{X}\right|\left|\tilde{A}\right|}{s^2}\right) \quad [S5]$$

where $I_0(\cdot)$ is the zeroth-order modified Bessel function of the first kind. According to the definition, $x_0=\frac{\left|\tilde{X}\right|}{s}$ and $a_0=\frac{\left|\tilde{A}\right|}{s}$, Eq. [S5] can be simplified as:

$$p_{X_0|A_0=a_0}\left(x_0\right)=2x_0e^{-x_0^2-a_0^2}I_0\left(2x_0a_0\right). \quad [S6]$$

https://dx.doi.org/10.21037/qims-21-1056

Derivation of Eq. [7]

By setting $iSNR \to 1$ in Eq. [6], the asymptotic decorrelation $\overline{D_{dy}}$ can be calculated as following:

$$\overline{D_{dy}} \to 1-\frac{\pi}{4}\int_0^{+\infty}\left[L_{0.5}\left(-a_0^2\right)\right]^2\delta\left(a_0\right)da_0 = 1-\frac{\pi}{4}\left[L_{0.5}\left(-a_0^2\right)\right]^2 = 1-\frac{\pi}{4}\approx 0.22, a.s., \quad [S7]$$

where the Rayleigh distribution $p_{A_0}\left(a_0\right)=\frac{2iSNR\cdot a_0}{1-iSNR}e^{-\frac{iSNR}{1-iSNR}a_0^2}$ approaches the delta function $\delta(a_0)$ when iSNR approaches 1.

Derivation of Eq. [10]

Given the normalized amplitude of the noiseless OCT signal a_0, the PDF of the decorrelation $D\left(x_0\left(t\right)\right)=1-iSNR^*x_0\left(t\right)\sqrt{2SNR^*-x_0^2\left(t\right)}$ for OCT signals in static region can be expressed as a function of $x_0(t)$:

$$p_{D\left(x_0(t)\right)\left|SNR^*\right.}\left(x_0\left(t\right)\right)=p_{X_0\left|A_0=a_0\right.}\left(x_0\left(t\right)\right)p_{X_0\left|A_0=a_0\right.}\left(x_0\left(t+1\right)\right)\sqrt{1+\left(\frac{\partial x_0\left(t+1\right)}{\partial x_0\left(t\right)}\right)^2}. \quad [S8]$$

Furthermore, a_0 follows a Rayleigh distribution determined by the local SNR. Taking this factor into consideration, the complete expression of Eq. [S8] is given by:

$$p_{D\left(x_0(t)\right)\left|SNR^*\right.}\left(x_0\left(t\right)\right)=\int_0^1 p_{isnr}\left(iSNR\right)diSNR\int_0^{+\infty}p_{A_0}\left(a_0\right)da_0$$

$$p_{X_0\left|A_0=a_0\right.}\left(x_0\left(t\right)\right)p_{X_0\left|A_0=a_0\right.}\left(x_0\left(t+1\right)\right)\sqrt{1+\left(\frac{\partial x_0\left(t+1\right)}{\partial x_0\left(t\right)}\right)^2}. \quad [S9]$$

https://dx.doi.org/10.21037/qims-21-1056